H-α Emitting Galaxies at z $\sim$ 0.6 in the Deep And Wide Narrowband Survey

by

Alicia Gonzalez

A Thesis Presented in Partial Fulfillment
of the Requirements for the Degree
Master of Science

Approved March 2017 by the
Graduate Supervisory Committee:

James Rhoads, Co-Chair
Sangeeta Malhotra, Co-Chair
Nathaniel Butler
Rolf Jansen

ARIZONA STATE UNIVERSITY

May 2017

ABSTRACT

New measurements of the Hα luminosity function (LF) and star formation rate (SFR) volume density are presented for galaxies at z$\sim$0.62 in the COSMOS field. These results are part of the Deep And Wide Narrowband Survey (DAWN), a unique infrared imaging program with large areal coverage ($\sim$1.1 deg^2 over 5 fields) and sensitivity ($9.9 \times 10^{-18} erg/cm^2/s$ at 5σ).

The present sample, based on a single DAWN field, contains 116 Hα emission-line candidates at z$\sim$0.62, 25% of which have spectroscopic confirmations. These candidates have been selected through comparison of narrow and broad-band images in the infrared and through matching with existing catalogs in the COSMOS field.

The dust-corrected LF is well described by a Schechter function with $L_* = 10^{42.64\pm0.92}$ erg s^{-1}, $\Phi_* = 10^{-3.32\pm0.93}$ Mpc^{-3} ($L_*\Phi_* = 10^{39.40\pm0.15}$), and $\alpha = -1.75 \pm 0.09$. From this LF, a SFR density of ρ_{SFR}=$10^{-1.37\pm0.08}$ M$_\odot$ yr^{-1} Mpc^{-3} was calculated. An additional cosmic variance uncertainty of $\sim$ 20% is also expected. Both the faint end slope and luminosity density that are derived are consistent with prior results at similar redshifts, with reduced uncertainties.

An analysis of these Hα emitters' sizes is also presented, showing a direct correlation between the galaxies' sizes and their Hα emission.

To my two families, at both sides of the Atlantic ocean.

ACKNOWLEDGMENTS

This work would not be possible without the guidance and support from my advisors, my thesis committee, my coworkers, and family and my friends all over the world.

First of all I would like to acknowledge my advisors Profs. James Rhoads and Sangeeta Malhotra. For the past four years they have not only helped me grow as an astrophysicist, but also as a person. All that I have learned will stay with me for the rest of my life. I also have to acknowledge Prof. Sara Walker, for showing me the beauty of polymers and computational astrobiology.

I would also like to thank my committee members, Profs. Nat Butler and Rolf Jansen, for not only jumping in with such short notice but still be of invaluable help for the last stages of this work, along with Profs. Hilairy Hartnett and Jenny Patience, for being part of my original committee.

I have to thank all my lab-mates, now friends, for making not only a great work atmosphere, but also making the lab an enjoyable place to spend my time at. Thank you John, for endless hilarious conversations and proctoring support. Thank you Tianxing for being an example of hard work and true friendship. And thank you Santosh, Lucia, Keunho, Bhavin, Karen and Tilvi for being the best people I could have asked to work with.

I also want to thank all the wonderful women of Mu Epsilon Theta for their unconditional support for the past three years. I would not be where I am now without the love and prayers of my sisters. I want to specially thank Jenna, Flow, Becca, Paola, Daniella and Kat, for always being there for me.

I would not be the same without all the people at the All Saints Catholic Newman Center, especially Sr. Mary Eileen and Amber Ray, who have been a great example of Catholic faith and the best role models I could ever find. I also have to thank the

Ruiz family for taking such good care of me all these years.

I can't thank Vu enough for everything he has done and keeps doing for me every single day: I don't know where I would be without your love and I can't wait to see what God's plan for us is.

I also have to thank Domino and Lyra for being my favorite (furry) roommates and making my life fluffier and cuter.

Last but not least I would like to thanks my parents for being there for me at all times, from the time I decided to embark on this graduate school adventure. Thank you all!

We thank NOAO for the generous allocation of observing time for the DAWN survey, and the Kitt Peak staff for their expert support of DAWN observations. We thank Kimberly Emig, Raviteja Nallapu, Emily Neel, Mark Smith, Stephanie Stawinski, Jacob Trahan, Nicholas Valverde, and Trevor Van Engelhoven for their help with DAWN survey observing runs. We thank NSF grant AST-0808165 for support of our custom filter purchase, and AST-1518057 for support of data analysis.

TABLE OF CONTENTS

CHAPTER Page

LIST OF TABLES

LIST OF FIGURES

Chapter 1

INTRODUCTION

The Balmer α line of hydrogen (Hα, the $n = 3 \rightarrow 2$ electronic transition of neutral hydrogen) is the gold standard of star formation rate indicators. It is produced as recombination radiation when hydrogen is ionized by UV radiation from young, massive stars. It can be used to efficiently identify small star-forming galaxies as the correspondence between Hα luminosity and SFR density has been accurately calibrated (Kennicutt, 1998). The Hα line is also a valuable redshift tracer, and will be used extensively to get redshifts by Euclid (Laureijs et al., 2011) and WFIRST (Spergel et al., 2015).

Narrow-band surveys are useful for finding emission-line galaxies at various redshifts. The Deep And Wide Narrow-band survey (DAWN) is a new 1.06 μm narrow-band survey that enables a uniquely sensitive search for these objects. The filter used in this survey detects mainly four lines that tend to be strong in emission line galaxies: Lyα, Hα, [OIII] and [OII], each of them at a different redshift. Different lines can be studied as proxies for different properties of galaxies. In this paper we focus on the Hα line where it enters the DAWN survey's narrowband filter at redshift $z = 0.62$.

To find emission-line galaxies, we use a broad-band and a narrow-band filter in the infrared. Given that the Earth's atmosphere greatly emits infrared radiation, we can only work on those infrared bands where the atmosphere's emission doesn't overpower the incoming light. In order to compare the images obtained with both filters, the narrow-band wavelength range has to be as close as possible to the broad-band filter range. In this case we are using a broad J-band filter (1.166-1.338 μm) and a custom-made narrow band filter centered at 1.066 μm. The qualitative process of selection consists of looking for objects that appear much brighter in the narrow-band filter than in the broad-band filter.

Once a candidate selection has been done, spectroscopic confirmation of a subset of candidates is necessary to confirm that the objects are indeed emission line galaxies and also to determine which line has been detected. Once we know which line we are looking at, the redshift of the galaxy can be easily determined.

Several surveys (Villar et al. (2008), Ly et al. (2011), Sobral et al. (2013)) have successfully studied the brightest end of the luminosity function of Hα emitters at similar redshifts to that explored in this paper, but the faintest end is less well studied. This paper fills that void, extending the luminosity function to fainter luminosities and helping extend the number of Hα measurements of the SFR density.

Throughout the paper, we adopt a Λ-CDM "concordance cosmology" with $\Omega_M = 0.27$, $\Omega_\Lambda = 0.73$, and $H_0 = 71\,\mathrm{km\,s^{-1}\,Mpc^{-1}}$.

Chapter 2

DESCRIPTION OF THE SURVEY AND COMPARISON WITH PREVIOUS SURVEYS

This paper is part of the Deep and Wide Narrow-band survey (DAWN), which is a uniquely deep survey that stands out for its sensitivity and area coverage. It was done using a custom-made narrow-band filter, centered at 10660 $\AA$ and 35 $\AA$ wide. DAWN was an NOAO survey project that used the 4-meter Mayall telescope at Kitt Peak National Observatory (Arizona) equipped with the NEWFIRM instrument (Probst et al. (2004), Probst et al. (2008)). This survey was approved as a long-term project and awarded 40 nights over the course two years, starting in the Fall of 2013. A survey extension was granted for the Fall of 2015, and 13 nights were awarded for that semester.

In this survey five fields were observed (COSMOS, UDS, EGS, MACS0717 and CFHTLS-D4). The observing times for this fields ranged from 20 hours for the the CFHTLS-D4 field to 83 hours for the UDS field.

A similar survey, NewHα (Ly et al., 2011) designed to detect Hα emitters at z$\sim$0.8 took place recently using the same instrument and a narrow-band filter centered at λ=11800 Å. This survey reached a limiting flux of $1.9 \times 10^{-17} erg/cm^2/s$ (AB magnitude of 23.63-23.74) at a 3σ level, equivalent to a 5σ detection of $2.85 \times 10^{-17} erg/cm^2/s$. If we compare these numbers to the DAWN survey, which has a 5σ detection of $9.9 \times 10^{-18} erg/cm^2/s$ in its deepest field, we can see that the DAWN survey reaches objects $\sim$ 3 times fainter.

The NewHα survey covers a comoving volume of $9.12 \times 10^4\, h_{70}^{-3}\, Mpc^3$ at z $\sim$ 0.8 while DAWN covers $2.83 \times 10^4\, h_{70}^{-3}\, Mpc^3$ (Wright, 2006). This means that the NewHα

survey covered a volume approximately 3 times bigger than the DAWN survey. However, despite surveying a greater volume, it can't detect the faintest objects.

Another recent related survey has been HiZELS (High-Z Emission Line Survey, Sobral et al. (2013)). This survey was designed to detect Hα emitters at z=0.4, 0.84, 1.47 and 2.23. For the detection of z$\sim$0.4 objects, they used the Suprime-cam on the Subaru Telescope at Mauna Kea Observatory (Hawaii) and a narrow-band filter centered at λ=9196 Å. This section of the survey reaches a limiting flux of $\sim 3 \times 10^{-17} erg/cm^2/s$ (AB magnitude of $\sim$24.4) at 3σ in the COSMOS field, equivalent to a 5σ detection of $\sim 5 \times 10^{-17} erg/cm^2/s$. It covers a comoving volume of $10.2 \times 10^4\, Mpc^3$. This means that, this survey covers a greater volume than DAWN ($\sim$3.8 times higher), but it can't detect objects as faint.

For objects at z$\sim$0.84, HiZELS used the Wide Field CAMera (WFCAM) on the United Kingdom Infrared Telescope (UKIRT), also at Mauna Kea Observatory, and a narrow-band filter centered at λ=12110 Å. At this redshift the survey reaches a limiting flux of $\sim 7.7 \times 10^{-17} erg/cm^2/s$ (AB magnitude of $\sim$22.9) in the COSMOS field, equivalent to a 5σ detection of $\sim 1.3 \times 10^{-16} erg/cm^2/s$. It covers a comoving value of $1.9 \times 10^5\, Mpc^3$, $\sim$6.7 times the volume covered by DAWN, but despite its large volume coverage, DAWN can detect objects $\sim$13 times fainter.

A summary of the specifications of these surveys can be found in Table 2.1.

Table 2.1: Specifications for Hα Surveys

Survey	**z**	**V** ($\mathbf{Mpc^3}$)	$\mathbf{f_{lim}(erg\ s^{-1}cm^{-2})}$	$\mathbf{L_{lim}(erg\ s^{-1})}$	$\mathbf{\Delta\lambda_{filter}}$(**Å**)
DAWN	0.62	2.83×10^4	9.9×10^{-18}	1.6×10^{40}	35
(this work)					
	0.16	1.0×10^4	6×10^{-17} (3σ)	4.2×10^{39} (3σ)	61
WySH	0.24	1.8×10^4	3.2×10^{-17} (3σ)	5.5×10^{39} (3σ)	58
(Dale et al., 2010)	0.32	-	2.8×10^{-17} (3σ)	9.4×10^{39} (3σ)	60
	0.40	-	2.2×10^{-17} (3σ)	1.2×10^{40} (3σ)	59
	0.4	5.13×10^4	5.9×10^{-18}	3.3×10^{39}	132
HiZELS	0.84	14.65×10^4	3.8×10^{-16}	1.3×10^{42}	150
(Sobral et al., 2013)	1.47	33.96×10^4	8.6×10^{-17}	1.16×10^{42}	211
	2.23	38.31×10^4	4.1×10^{-17}	1.55×10^{42}	210
NewHα	0.8	9.12×10^4	1.9×10^{-17}	5.7×10^{40}	111
(Ly et al., 2011)					
Villar et al. (2008)	0.84	13×10^4	5×10^{-17}	1.7×10^{41}	120
Hayes et al. (2010)	2.2	-	6.85×10^{-18}	2.5×10^{41}	190

Chapter 3

OBSERVATIONS AND DATA REDUCTION

3.1 Data Acquisition

The data for this project has been taken with the NOAO Extremely Wide-Field Infrared Imager (NEWFIRM; Probst et al. (2004, 2008)) on the 4-m Mayall telescope (Kitt Peak National Observatory, Arizona, USA). This instrument images a 28x28 arcmin field of view at 0.4 arcsec/pixel with a 35 arcsec wide chip gap, and covers infrared wavelengths between 1 μm and 2.4 μm.

After taking different sample images with different settings, we decided it was best to take 600s exposures with 16 Fowler samples, and 8 digital averages per pixel during readout, in a random dithering pattern. In order to minimize the effect of the chip gap in the data a dither of $45'' \times 45''$ was used.

The current narrow-band data available and analyzed is equivalent to an integration time of around 81 hours in the COSMOS field (RA $\sim 150°$, DEC $\sim +2°$). This time corresponds to a 5σ limit detection of $9.9 \times 10^{-18} erg/cm^2/s$ (AB magnitude $\sim$23.8).

The J-band image we use throughout this project comes from the UltraVISTA survey DR3 (2016), based on data products from observations made with ESO Telescopes at the La Silla Paranal Observatory under ESO programme ID 179.A-2005 and on data products produced by TERAPIX and the Cambridge Astronomy Survey Unit on behalf of the UltraVISTA consortium (McCracken et al., 2012).

3.2 Stacking

Data reduction has been done with a combination of the NEWFIRM pipeline (Swaters et al., 2009) and our own. Resampled images (calibrated, sky-subtracted, re-projected and resampled) provided by the NEWFIRM pipeline along with their counterpart bad pixel masks were used as a starting point.

Approximately a quarter of the images acquired have issues that make them unusable. Most of those images include condensation patterns or were taken in too poor weather conditions to be of any use.

We stacked the remaining high quality images using the imcombine task on IRAF v2.16 with an average as the combination operation, and "sigclip" as the rejection parameter at a 3σ level. This rejection parameter rejects pixels using a sigma clipping algorithm that minimizes the number of cosmic rays that make it to our final stack.

3.3 Source Detection

Once the images are calibrated, the next step is to detect all the sources present in the narrow-band image. However, before this step it is necessary to get rid of the parts of the images that are too noisy to work, in this case mostly the outskirts and those parts corresponding to regions of elevated dark current or read noise. This process will minimize the number of false detections.

In order to be able to directly compare the narrow-band and the broadband image, the broad-band images are resampled onto the coordinate grid of the narrow-band image. More detail about the DAWN survey can be found in J. Rhoads et al. (2017, in preparation).

The objects are identified in the narrow-band image using SourceExtractor v2.8.6 (Bertin & Arnouts, 1996) in dual image mode to measure their fluxes in other pass-bands. The dual image mode consists on finding all the objects in one image, then applying the apertures and positions found on another image. Therefore, the first image is used for the detection of the sources and the second image for the photometry. Applying this method twice, once for each science image (with the narrow-band image used both times as the detection image) renders two catalogs, one per image, with the flux (and error) for all the sources. The same source will have the same ID in both files, making it simple to identify the same object in both images.

SourceExtractor analyses an image in six steps: estimation of the sky background, thresholding, deblending, filtering of the detections, photometry and star/galaxy separation.

The sky subtraction is done with the AUTO mode in a background mesh of 64 pixels and a median filter of 3x3 pix. Before extracting the objects a convolution filter is applied to the image. The specific one employed here is a 7x7 pix convolution mask of a gaussian PSF with FWHM = 3.0 pix (1.2"). The parameter settings applied require a detection of 0.7σ per pixel in each of 7 connected pixels in order to consider an area of the image an object. A threshold of 64 with a contrast parameter of 0.001 is applied in order to deblend objects. No weighting is applied.

SourceExtractor detected 51695 objects within our narrow-band image. However, after removing the parts of the image that were excesively noisy, only 17121 objects remained.

3.4 Significance of the Sources

By setting the specific parameters explained in the previous section, we make sure that all the sources in the images are detected. However, the catalogs generated also label certain areas of elevated noise as sources, when they are not so. Another important step in the sample selection process is then getting rid of all these false detections.

The criterion established to label a source as real is that it is a 5σ detection, that is, that it has a signal to noise ratio of 5. The application of this criteria gives us an expected number of false positives of the order of 1 object, assuming Gaussian noise.

Both the signal and the noise are calculated by SourceExtractor in a 5 pixel diameter aperture around the source. The signal is the flux within that aperture and the noise its RMS error. 13844 sources, out of the 17121 that SourceExtractor detected on the clean areas of the image, passed this criteria.

3.5 Selection of Sources

Given the different natures of the narrow-band and the broadband images, it was necessary to calibrate both of them before they could be directly compared to each other. This is made by adjusting the zero point in the broadband image so that the average (J-1.066 μm) color is 0. Figure 3.1 shows the application of these selection criteria to the detected sources.

In order to separate the emission-line objects from the rest, two criteria are taken into account. First of all, only sources which are much brighter in the narrow-band image than in the broad-band are considered potential emission-line objects. These criteria are virtually identical to those employed in previous, similar surveys (Ly et al. (2011), Sobral et al. (2013), Villar et al. (2008)).

The criterion for the mean flux density in the narrow-band and J-band filters (f) is:

$$\frac{f(NB\ \ 1066)}{f(J)} \geq 1.5$$

which equals to an equivalent with of 18 $\mathring{A}$ in observer frame.

903 sources from our catalog pass this criteria. Then, from these objects, only

those who show an important color significance are taken into account:

$$\frac{f(NB1066) - f(J)}{\sqrt{(\sigma_{f(NB\ 1066)})^2 + (\sigma_{f(J)})^2}} \geq 2$$

After the application of these criteria, the emission-line candidates catalog consisted of 847 sources. A complete list of how many sources passed each criterion can be found in Table 3.1.

3.6 Photometric Calibration

In order to calibrate the images, so we could get the true magnitude of the sources, we used the UltraVISTA K-selected Catalog v4.1 (McCracken et al., 2012). This catalog contains AB magnitudes in several broad-band filters, including J and Y, the ones whose central wavelengths (1.252 μm and and 1.020 μm respectively) are closest to that of our narrow-band filter. In order to get a magnitude closer to that of our filter, that permits a more accurate calibration of our data, an interpolation between the magnitudes in these filters was employed. These interpolation led to an artificial 1.066 μm continuum magnitude, directly comparable to our data:

$$\begin{aligned} m_{UV,1066} &= m_{UV,Y} + \frac{\lambda_J - \lambda_{1066}}{\lambda_J - \lambda_Y} \left(m_{UV,J} - m_{UV,Y}\right) \\ &\approx m_{UV,Y} + 0.2 \left(m_{UV,J} - m_{UV,Y}\right) \end{aligned}$$

The UltraVISTA catalog contains both stars and galaxies. However, for calibration purposes, only the stars were used, that is objects with the parameter $STAR$=1 in the UltraVISTA catalog (McCracken et al., 2012).

This catalog was compared to the one generated from our images in order to identify the objects present in both. Out of our catalog, only the objects that Source-Extractor marked as non-flagged stars ($CLASS\_STAR$=1 and $FLAGS$=0) were considered.

The magnitudes in the UltraVISTA catalog are magnitudes inside a 2.1" aperture. Given the pixel scale of NEWFIRM, 0.4"/px, our magnitudes are calculated with an diameter aperture of 5 px, equivalent to 2".

Given the different nature of the catalogs, slight differences in the coordinates for the same object are expected. The criteria to consider an object present in both catalogs was that both its RA and DEC were within 1" of each other.

Once the conversion between aperture magnitudes and AB magnitudes is determined, magnitudes for all the detected sources are calculated. The limiting magnitude, that corresponding to an object with a 5 σ detection, was calculated by averaging the magnitudes for all objects with signal to noise between 4.8 and 5.2. The resulting limiting magnitude is found to be 23.79, which for a filter with $\Delta\nu_{filter} = 9 \times 10^{11} Hz$ corresponds to a limiting line flux of:

$$\begin{aligned} f_{lim} &= (3600 \times 10^{-0.4 \times m_{AB}} \ Jy) \times (10^{-23} \ erg/cm^2/s/Hz/Jy) \times \Delta\nu_{filter}(Hz) \\ &= 9.9 \times 10^{-18} erg/cm^2/s \end{aligned}$$

3.7 Comparison with Photometric Redshift Catalogs

For the COSMOS field, we compared the emission-line candidates with the "COSMOS2015 Catalog" (Laigle et al., 2016). This is the most complete photometric redshift catalog available for this area of the sky, and it completely overlaps with our survey in this field.

This catalog includes around 600,000 objects within a 1.5 square degree field up to magnitude 24.0 in the K_S filter (λ_c= 21539.9 Å). These objects are imaged using most of the major space-based telescopes plus a number of large ground-based telescopes. It includes magnitude measurements of these objects in different regions of the electromagnetic spectra, from the x-ray to the far infrared, along with photometric redshifts, and their corresponding confidence intervals.

We also compared our candidate list with the "COSMOS Photometric Redshift Catalog" (Ilbert et al., 2009) and the "COSMOS January 2006 Photometry Catalog" (Capak et al., 2007). These catalogs correspond to previous releases of COSMOS optical and NIR data. Even if these catalogs are previous versions of the one mentioned above, they still contains some objects not included in later editions.

We compared our list of objects to these catalogs, trying to find corresponding objects. We considered that one of our objects matched one in the catalog if the coordinates were less than 1" apart.

From our list of 847 emission-line candidates, 741 matched an object in at least one of the catalogs.

3.8 Comparison with Spectroscopic Redshift Catalogs

We also compared the list of emission-line candidates in the COSMOS field with both the zCOSMOS (Lilly et al., 2007, 2009) and the PRIsm MUlti-object Survey (PRIMUS; Coil et al. (2011); Cool et al. (2013)) spectroscopic redshift catalogs.

The zCOSMOS survey includes 10,000 I-band selected sources at $z \leq 1.2$. The PRIMUS survey includes almost 30,000 sources up to $z \sim 1$.

The comparison of our emission-line candidates catalog and these catalogs yield 115 matches with the zCOSMOS catalog and 222 matches with the PRIMUS catalog. Combining these two lists of matches and discarding spectroscopic catalog entries that lacked a published, secure redshift, our final list included 269 objects with an available spectroscopic redshift. These 269 make our spectroscopic redshift emission-line candidates list. All these sources also have an available photometric redshift.

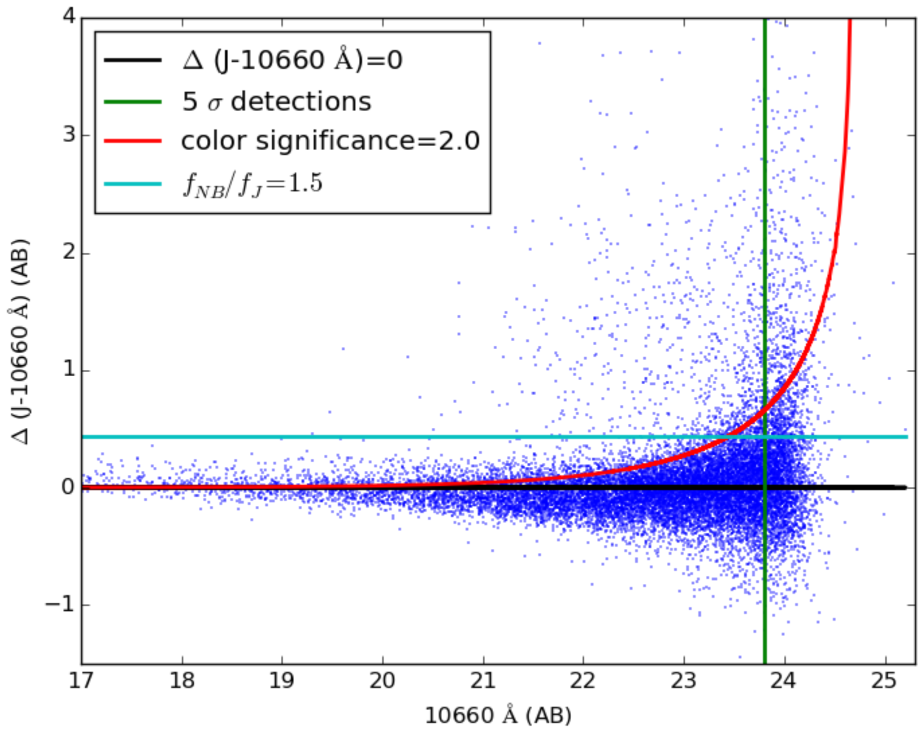

Figure 3.1: Emission-line Objects Selection Criteria
Color-magnitude diagram showing the selection criteria for narrow-band excess emitters: significance of the detections, color excess and color significance.

Table 3.1: Selection Criteria

Number of sources remaining after each selection criteria was applied

Criteria	**Sources**
Detected	51695
Geometric cut	17121
5σ detections	13844
Flux ratio	903
Color significance	847
Photometric redshift match	751
Spectroscopic redshift match	269
Hα emitters	116

Chapter 4

Hα CANDIDATE SELECTION

The Hα emission-line candidates were selected from both the photometric redshift and the spectroscopic redshift emission-line candidates lists. Given the central wavelength of our narrow-band filter, 10660 $\mathring{A}$, and its width, 35 $\mathring{A}$, we expect to find Hα emission-line objects between redshifts z=0.616 and z=0.631. Hα candidates would then be those objects whose redshift, photometric or spectroscopic, falls between these limits. However, the filter employed is not a perfect square wave, and also the angle of incidence of the photons on the filter results in a bandpass shift towards bluer wavelengths near the edge of the field. These issues, along with the uncertainty of the photometric redshifts, suggest the selection criteria stated above is too strict.

Photometric redshifts from the "COSMOS2015 Catalog" (Laigle et al., 2016) catalog include error bars at the 68% confidence level, even if previous versions of said catalog included both at the 68% and 99% level. As some objects appear in previous versions of the catalogs, but not in the latest one, we assumed that the 99% confidence bars would be approximately twice as big as the 68% ones, given us a way to directly compare both kinds of object.

Spectroscopic redshifts from the zCOSMOS and PRIMUS catalogs do not include explicit error bars, instead they are classified as very secure, secure, best guess, probable and insecure based on their agreement with redshifts independently derived from repeat observations of the same galaxy and the consistency with photometric redshifts derived from the COSMOS photometric data. Only those redshifts considered very secure or secure were used in the end.

As a first selection criteria, we selected those objects whose photometric redshift was compatible with the Hα line but not with any other line (e.g. [OIII] at λ=5007 Å). This gave us a list of objects with photometric redshifts ranging between z=0.09 and z=0.75. However, there were some objects with photometric redshifts within this range that did not pass this criteria due to having small error bars. We looked at those objects' redshifts in previous releases of the COSMOS photometric redshift catalog and found out that most of those objects would have passed this criteria. Therefore, our candidate list includes all objects selected as emission-line objects that have a photometric redshift between 0.09 and 0.75. This list is made of 116 objects, out of which 50% fall between z=0.60 and z=0.65, and 85% fall between z=0.55 and z=0.70. From this 116 objects, 22 of them also have an available spectroscopic redshift.

Figure 4.1 shows the photometric distribution for the candidate list along with the transmission of our narrow-band filter.

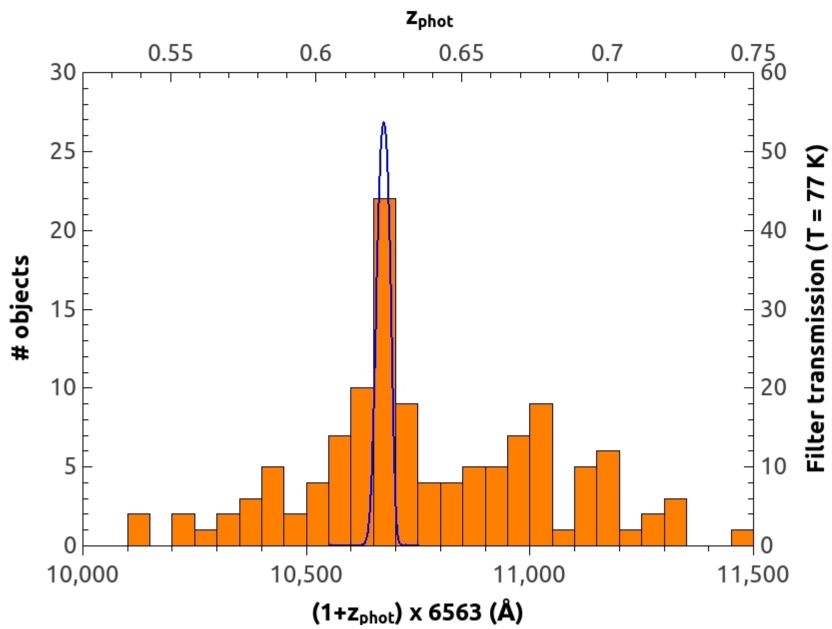

Figure 4.1: Redshift Distribution
Photometric redshift distribution for the Hα candidates along with the transmission of our narrow-band filter, which shows the theoretical position of Hα emitters observed with such filter ($\lambda = 6563\mathring{A}\ (1 + z_{phot})$ for the sources that don't have an available spectroscopic redshift).

Chapter 5

CALCULATION OF Hα LUMINOSITIES

In order to obtain the intrinsic Hα luminosity from the observed line luminosity, this must be corrected for contamination of the flux by the [NII] $\lambda\lambda$6548,6584 lines, located close to the Hα line in the spectra, and for attenuation due to the dust present in the galaxies. We apply commonly employed corrections that are adequate for ensemble populations despite having large scatter when applied to individual objects.

5.1 [NII] Contamination

Most narrow-band surveys use filters that are broad enough to include both the [NII] $\lambda\lambda$6548,6584 lines along with the Hα line at λ6563 and include corrections that account for the presence of both lines. Villar et al. (2008), Ly et al. (2011) and Sobral et al. (2013) adopt an EW-dependent Hα/[NII] ratio derived from Villar et al. (2008) determination of the mean relationship between the rest-frame EW of Hα + [NII]λ6583 and the Hα/[NII] flux ratio. This correction assumes that this relation doesn't evolve with redshift.

However, our narrow-band filter is narrow enough that at z $\approx$ 0.6 only includes flux from one of the [NII] $\lambda\lambda$6548,6584, making the corrections needed intrinsically different than those in other surveys.

Not having a spectroscopic redshift for all the sources implies that we can't know which [NII] line is the source of contamination in each object, so calculating an individual correction for each object is not possible.

The ratio of Hα flux to [NII] (including both lines) in typical galaxies is considered to be around 2.3 (Ly et al., 2011). The λ6584 line of [NII] has an intensity of roughly a third of Hα and at z$\sim$ 0.6 falls 33 $\mathring{A}$ away from the Hα line. With a filter 35$\mathring{A}$ wide, whenever the Hα line falls in the center of the filter (>50% transmission), this [NII] will fall on the wings of the filter. The λ6548 [NII] line has an intensity of around 10% of the Hα line and falls 24 $\mathring{A}$ away at this redshift, placing it at a reasonably transmissive part of the filter when the Hα line is in the redder portion of the filter.

Considering all this, we assumed a constant correction of 10% of the line flux. Even if this correction is not accurate for individual objects, it fits within our level of precision for a sample as big as ours.

5.2 Dust Attenuation

In order to correct for dust attenuation, we follow the luminosity-dependent extinction relation used in Ly et al. (2011) following Hopkins et al. (2001):

$$\begin{aligned} log\,[SFR_{obs}(H\alpha)] &= log\,[SFR_{int}(H\alpha)] \;-\; 2.360 \\ &\quad \times\; log\left[\frac{0.797\; log\,[SFR_{int}(H\alpha)] \;+\; 3.786}{2.86}\right] \end{aligned}$$

where SFR is expressed in $M_{\odot}$/yr.

This relation is based on experimental data (Calzetti et al. (1995), Wang & Heckman (1996)) that shows that objects with higher FIR luminosity have both a high presence of dust and a high SFR. As the Hα luminosity directly correlates with SFR, these results imply that more luminous galaxies within our survey are more affected by dust extinction.

Using the same correction approach as previous works facilitates the direct comparison of results.

Figure 5.1 shows both the narrow-band AB magnitude and observed equivalent width (after [NII] contamination and dust attenuation corrections are applied) distribution for out Hα candidate list.

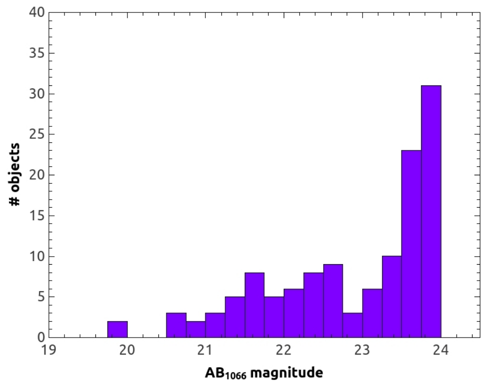

(a)

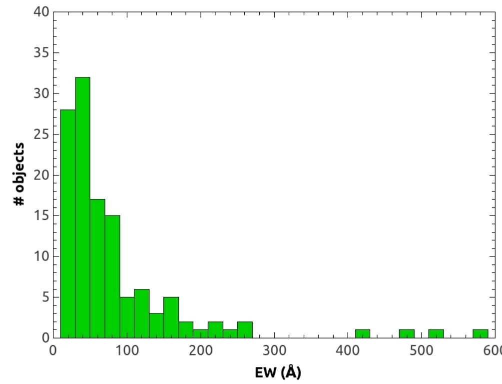

(b)

Figure 5.1: Properties of Hα Candidates
AB magnitude and observed equivalent width distributions of the Hα candidates

Chapter 6

COMPLETENESS

In order to accurately determine the detection limits of the DAWN survey it is necessary to estimate the completeness fraction, that is how the number of objects that our selection methods recover compare to the total number of existing objects. This completeness fraction will depend on both the luminosity and EW of the sources.

The approach to calculating the completeness fraction is to create artificial sources and superimpose them to our science image and repeat all the selection procedures explained in sections 3.3-3.5 in said image. A comparison between the number of sources added, and the number recovered that were not in the selection with only real objects will yield the recovery fraction. This artificial sources are created as extended sources with a two-dimensional gaussian shape having the same FWHM as compact galaxies in the survey ($\sim$ 1.2”).

We repeated this process once for each one of our 800 intervals of luminosity and observed EW, which ranged from $10^{38.7-42.7} L\odot$ in steps of 0.1 dex and an EW of 0-200 $\mathring{A}$ in 10$\mathring{A}$ steps. The nominal detection limits of this survey are $L_{lim} = 10^{39} L\odot$ and $EW_{lim} = 18\mathring{A}$, so these intervals assure we cover objects both close and far from the detection limits.

In each simulation, we generated 10,000 artificial galaxies, which corresponds to $\approx 20\%$ of the sources in the science image. For each artificial object, its narrow-band luminosity and EW are selected randomly from the L-EW interval they correspond to. The J-band luminosity is then derived from:

$$EW_{obs} = \Delta NB \, \frac{f_{NB} - f_J}{f_J - f_{NB}(\Delta NB/\Delta J)} = 35\mathring{A} \, \frac{f_{NB} - f_J}{f_J - f_{NB}(35\mathring{A}/1720\mathring{A})}$$

The artificial source fluxes are then scaled to counts using the appropriate zero points, and randomly scattered over the science images. Finally, the selection rules are applied to the resulting images.

For each simulation, we define a recovery fraction dependent on the number of objects recovered and the number of real and artificial objects in the image:

$$\kappa = 100 \times \frac{N_{detected} - N_{real}}{N_{artitificial}}$$

In the simulations with lowest EW the number of objects recovered was lower than in the science image with no added sources. Therefore, we assumed that due to an overcrowding of the image not all the real sources are recoverable and we took N_{real} as the lowest amount of objects recovered in the whole set of simulations instead of the number of real emission-line sources in the image.

This completeness correction was applied to each individual source in our H α sample according to its luminosity and equivalent width.

A summary of the completeness fraction as a function of luminosity and equivalent width can be found in Figure 6.1.

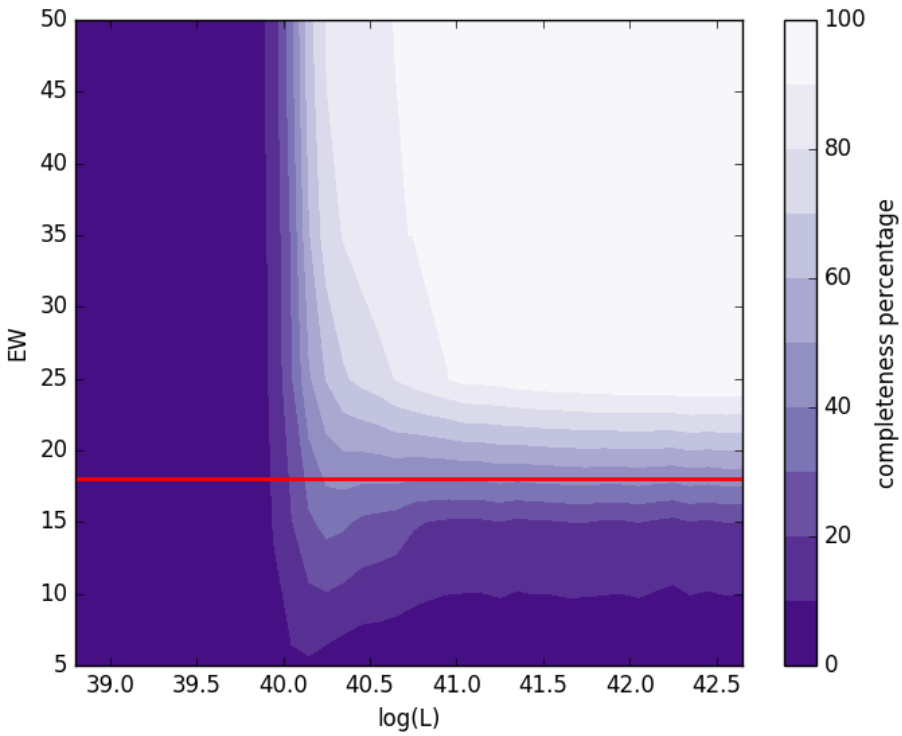

Figure 6.1: Completeness Percentage

Completeness percentage as a function of L and EW. The minimum EW detected in the DAWN survey is marked with a red line

Chapter 7

LUMINOSITY FUNCTION FITTING AND STAR FORMATION RATE DENSITIES

We construct our Luminosity Function binning our Hα sample in bins 0.3 dex wide in luminosity. Observed and extinction- and completeness-corrected number and number densities as a function of luminosity are listed in Table 7.1.

Our luminosity function is fitted to a Schechter function (Schechter, 1976) defined by the parameters ϕ_*, L_* and α:

$$\Phi(L)\, dL \;=\; \phi_* \Big(\frac{L}{L_*}\Big)^{\alpha} exp\Big(-\frac{L}{L_*}\Big)\, \frac{dL}{L_*}$$

In the log form, this equation translates into:

$$\Phi(L)\, dL \;=\; ln(10)\, \phi_* \Big(\frac{L}{L_*}\Big)^{\alpha+1} exp\Big(-\frac{L}{L_*}\Big)\, d(log\ L)$$

We assume that this function can be accurately used to model the distribution of Hα luminosities. This approach has also been extensively used in the past, which makes it ideal to compare our results to previous work (Villar et al. (2008), Ly et al. (2011), Sobral et al. (2013)).

In order to obtain the confidence range of the best-fitting Schechter parameters, we performed a Monte Carlo simulation to consider the full range of scatter in the extinction-corrected Hα LF. Each point in the binned luminosity function was randomly perturbed 2500 times following a Gaussian distribution, with the variances of the Gaussian drawn according to its error bars. Then, we calculated the best fit to a Schechter function for each of these simulatons using a χ^2 fit. It is worth noting that most of these fittings were more consistent with a power-law than with a Schechter function, as it can be seen in Figure 7.2. However, as the best fitting to our data corresponds to a Schechter function, and for easier comparison with previous work, we assumed that a Schechter function is the best fit to the data and not consider those simulations whose results are not consistent with such when computing the LF parameters.

The best-fitting parameters are determined to be $L_* = 10^{42.64\pm0.92}$ erg s^{-1}, $\Phi_* = 10^{-3.32\pm0.93}$ Mpc^{-3}, and $\alpha = -1.75\pm0.09$. The uncertainties in L^* and Φ^* are strongly anticorrealted, as seen in Figure 7.2.

The integrated Hα luminosity density can then be calculated from the Schechter parameters:

$$L(H\alpha) = \int_{L_{min}}^{\infty} L\ \Phi(L)\ dL = L^*\ \Phi^*\ \Gamma\Big(2+\alpha, \frac{L_{min}}{L^*}\Big)$$

The integrated Hα luminosity density can subsequently be converted into an SFR density following Kennicutt (1998): SFR(Hα)=7.9 $\times$ 10^{-42} L(Hα), where the SFR is given in M$_\odot$ yr^{-1} and the Hα luminosity is given in erg s^{-1}. We determine that the Hα SFR density is ρ_{SFR}=$10^{-1.32\pm0.08}$ M$_\odot$ yr^{-1} Mpc^{-3} down to L=0. If we calculate the SFR density down to our luminosity limit ($log(L_{lim}) = 40.16$) this result decreases to ρ_{SFR}=$10^{-1.42\pm0.08}$ M$_\odot$ yr^{-1} Mpc^{-3}.

In order to account for the presence of AGNs, we compared our catalog of Hα candidates to the XMM-Newton wide-field survey (Cappelluti et al., 2009) and the Chandra Cosmos Legacy Survey catalogs (Civano et al., 2016), but no matches were found (however, other DAWN objects identified as emission-line objects but not Hα emitters were identified in said catalogs). As no measurement of the X-ray emission of our candidates is available, we follow the approach described in Ly et al. (2011) and correct the value presented above by 11%. Similar approaches have been used in other surveys (e.g. Sobral et al. (2013) used a 10% correction up to z $\sim$ 1). Our total Hα SFR density is reduced then to ρ_{SFR}=$10^{-1.37\pm0.08}$ M$_\odot$ yr^{-1} Mpc^{-3} down to L=0

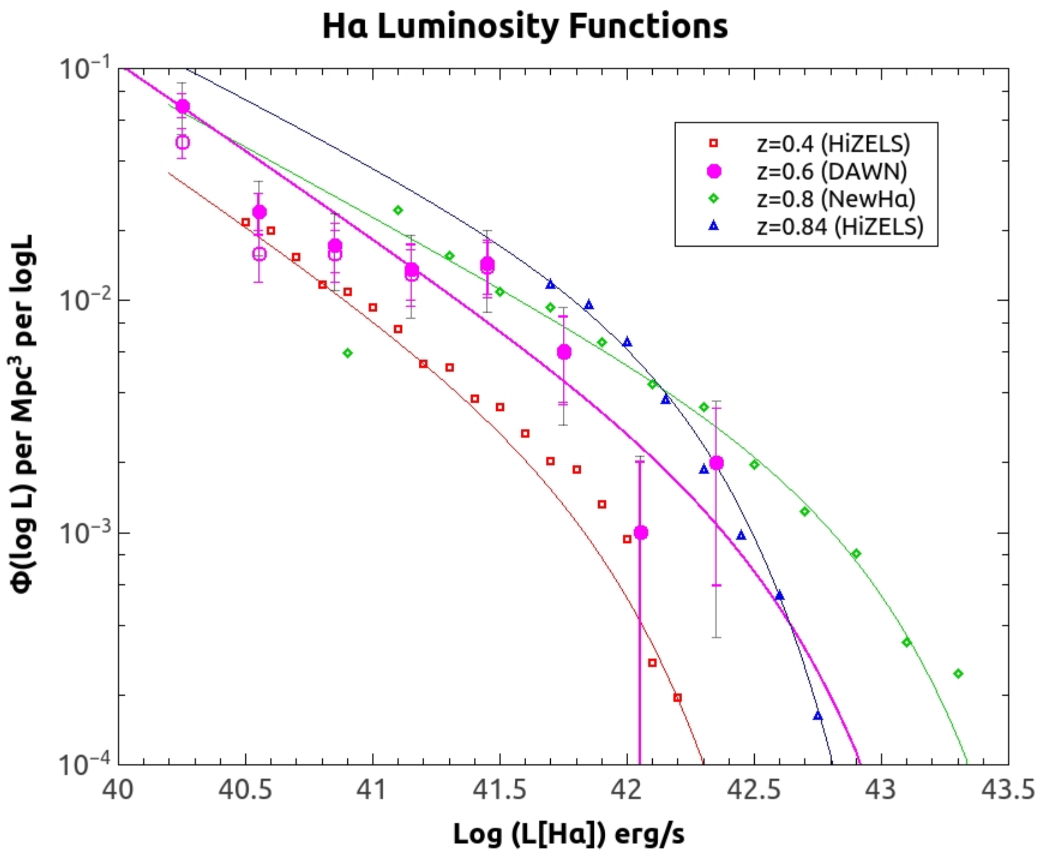

Figure 7.1: Hα Luminosity Function Compilation
Luminosity function for HiZELS (Sobral et al., 2013), NewHα (Ly et al., 2011) and DAWN surveys (this work). For the DAWN survey, magenta error bars show the Poisson error while black bars show the uncertainty due to cosmic variance.

and to ρ_{SFR}=$10^{-1.47\pm0.08}$ $M_{\odot}$ yr^{-1} Mpc^{-3} down to L=L_{min}.

Madau & Dickinson (2014) provides an experimental fit to the total SFR density as a function of redshift ($\psi(z)$). Following their procedure we obtain a total star formation density of $\psi = 10^{-1.27}$ $M_{\odot}$ yr^{-1} Mpc^{-3} at z$\sim$0.62. This result implies that galaxies like those in our sample account for roughly 80% of the total star formation rate density at z$\sim$0.62.

Table 7.1: Hα Luminosity Function

Extinction and completeness-corrected Hα Luminosity Function at z $\sim$ 0.62. Φ(log L) is normalized to $1 \times 10^{-2} Mpc^{-3} dex^{-1}$.

log(L[Hα])	**N$_{observed}$**	**N$_{corrected}$**	**Φ(log L)**
40.25	48	69	6.95 $\pm$ 0.83
40.55	16	24	2.45 $\pm$ 0.49
40.85	16	17	1.74 $\pm$ 0.42
41.15	13	13	1.38 $\pm$ 0.37
41.45	14	14	1.45 $\pm$ 0.38
41.75	6	6	0.61 $\pm$ 0.25
42.05	1	1	0.10 $\pm$ 0.10
42.35	2	2	0.20 $\pm$ 0.14

Table 7.2: Luminosity Function Parameters for Different Surveys

Survey	**z**	**L***	**Φ***	α
DAWN (this work)	0.62	42.64	-3.32	-1.75
WySH (Dale et al., 2010)	0.16	42.0	-3.05	-1.36
	0.24	41.8	-2.74	-1.41
	0.32	42.1	-2.77	-1.26
	0.40	42.2	-2.79	-1.14
HiZELS (Sobral et al., 2013)	0.40	41.95	-3.12	-1.75
	0.84	42.25	-2.47	-1.56
	1.47	42.56	-2.61	-1.62
	2.23	42.87	-2.78	-1.59
NewHα (Ly et al., 2011)	0.84	43.0	-3.2	-1.6
Villar et al. (2008)	0.84	42.97	-2.76	-1.34
Hayes et al. (2010)	2.2	43.07	-3.45	-1.6

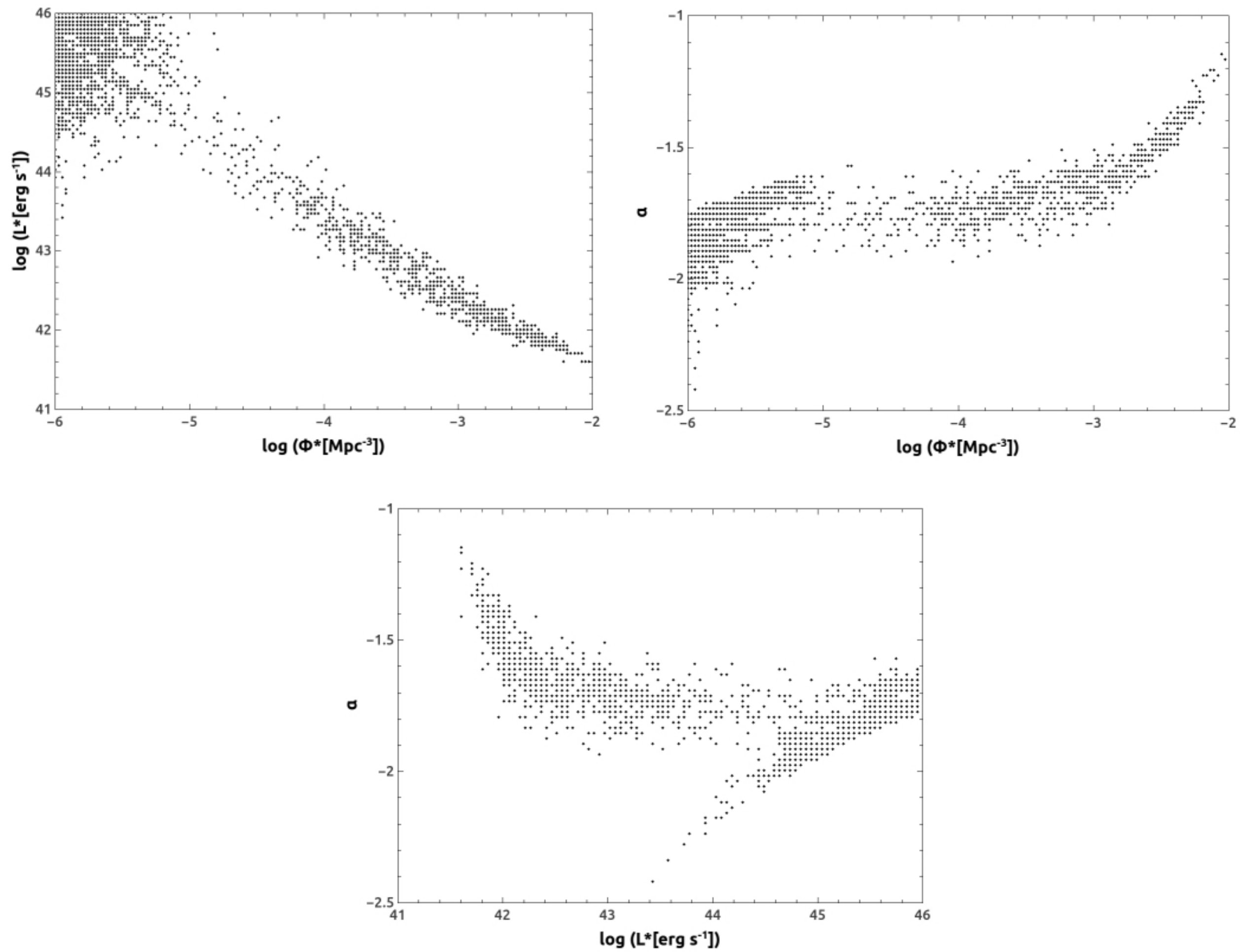

Figure 7.2: Luminosity Function Parameters
Best fit to the Schechter luminosity function parameters for our ∼2500 Montecarlo simulations.

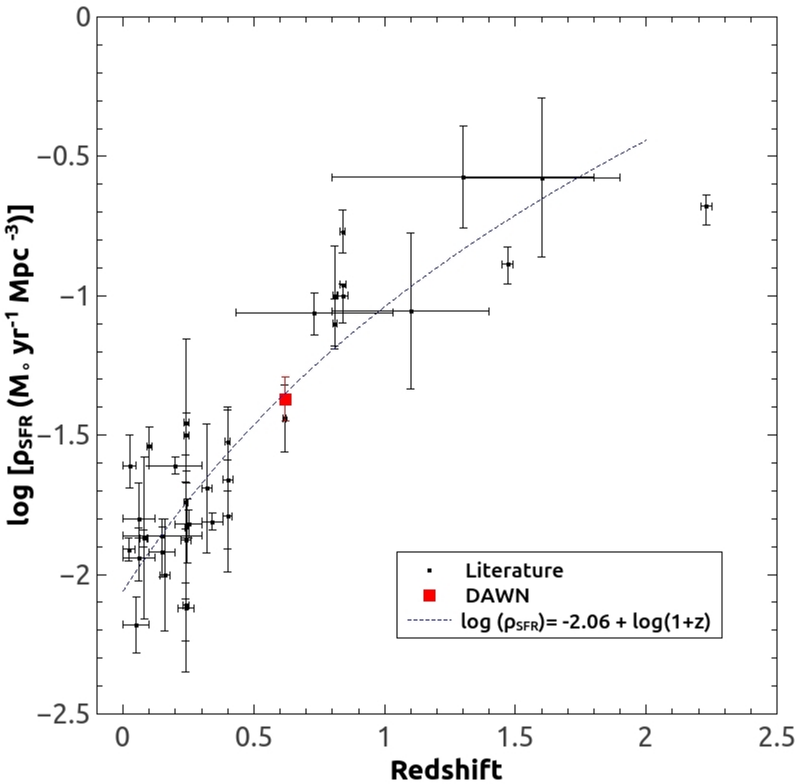

Figure 7.3: SFR Density from Hα Surveys.

Black circles are measurements from the literature (a combination of Table 5 of Ly et al. (2011) and Table 5 of Sobral et al. (2013), along with the result from Gómez-Guijarro et al. (2016)) and the red square is our measurement. The dashed blue line is the fit derived in Dale et al. (2010) for z<2. All the points include corrections for dust extinction, but other differences may not be fully accounted for.

Chapter 8

Hα SIZES

We compare our Hα sample with the "COSMOS ACS catalog" (Leauthaud et al., 2007) in order to obtain the sizes (half-light radii) of the emitters in our sample. Out of our 116 objects, 115 are found in said catalog.

We divide our sample in two sub-samples, according to the Hα luminosity of the sources. We have a faint sample containing 79 sources with log(L)$\leq$ 41.0 and a bright sample containing 36 sources with log(L) $>$ 41.0.

The median half-light radius for the whole sample is 0.27", while it is 0.22" for the faint sample and 0.39" for the bright sample. The interquartile range for the whole sample is 0.18"-0.38", while it is 0.17"-0.30" for the faint sample and 0.29"-0.54" for the bright sample. It can be seen that the dimmer objects also tend to be smaller, showing a correlation between luminosity and size in Hα emitters.

The size distribution for the full Hα sample along with that of the bright sample can be found in figure 8.1.

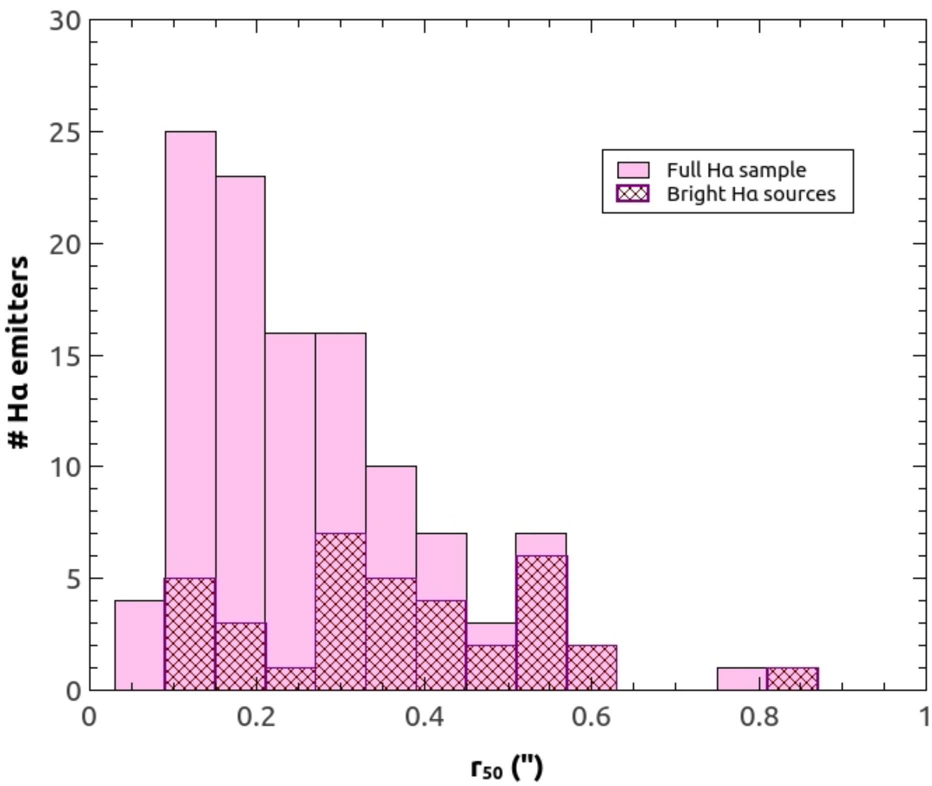

Figure 8.1: Size Distribution

Size distribution for the DAWN Hα sample along with the size distribution of those objects with log(L) $>$ 41.0.

Chapter 9

DISCUSSION

In Figure 7.1 we show the extinction and completeness-corrected LF for the DAWN survey, the NewHα survey and the HiZELS survey at z=0.4 and z=0.84. The LF function parameters for the three surveys can be found in Table 2.1. This figure includes both completeness-corrected and uncorrected DAWN data points, along with statistical uncertainties and cosmic variance related uncertanties calculated following Trenti & Stiavelli (2008).

The bright end of the luminosity function agrees with HiZELS (Sobral et al., 2013) at z=0.84, NewHα (Ly et al., 2011) at z=0.84, and Villar et al. (2008) also at z=0.84. The number density of objects obtained from the DAWN survey is consistent with that of all these surveys too.

However, the biggest strength of the DAWN survey is the tight constraint on the slope of the faint end of the LF, α. Our result is consistent with that of previous surveys at similar redshifts, but provides a smaller error bar due to reaching fainter objects. It is worth noting than although the value of α reported in Villar et al. (2008) is substantially higher, that value was fixed on their calculations due to a lack of faint data.

In Figure 7.2 we show our measurement for Hα SFR density along with a compilation of measurements from other surveys that have used that same emission line. The compilation was originally made by Dale et al. (2010) and reproduced and corrected for mistakes found in the original papers by Ly et al. (2011). We also add results presented in Sobral et al. (2013) and Gómez-Guijarro et al. (2016). The SFR density obtained from the DAWN survey is consistent with those of previous surveys at redshift $z < 2$, and refines our understanding with a more precise measureent than prior surveys at $0.5 < z < 0.8$.

Chapter 10

CONCLUSIONS

We have presented new measurements of the Hα luminosity function (LF) and SFR volume density for emission-line galaxies at z$\sim$0.62. These measurements are based on 1.06 μm narrowband imaging from the DAWN survey. This survey fills a gap in the redshift coverage for Hα luminosity function studies.

The DAWN survey has a 5σ emission-line flux depth of $9.9 \times 10^{-18} erg/cm^2/s$ and an area coverage of $\sim$0.22 deg^2 in the COSMOS field. We identified 847 narrow-band excess emitters above 5σ, and 116 of them were identified as Hα emission-line galaxies at z$\sim$0.62. This classification is done by comparison with both photometric and spectroscopic redshift catalogs.

We constructed the extinction and completeness-corrected Hα LF. Corrections for dust attenuation and [NII] contamination were applied. The LF is well described by a Schechter function with $L_* = 10^{42.64\pm0.92}$ erg s^{-1}, $\Phi_* = 10^{-3.32\pm0.93}$ Mpc^{-3}, $L_*\Phi_* = 10^{39.40\pm0.15}$ erg s^{-1} Mpc^{-3}, and $\alpha = -1.75 \pm 0.09$. This faint end slope, α, is consistent with but better constrained than earlier works at $0.4 < z < 0.85$.

Integrating the LF to L=0, we determine a SFR density of ρ_{SFR}=$10^{-1.37\pm0.08}$ M$_\odot$ yr^{-1} Mpc^{-3}. This luminosity density is consistent with the interpolation of prior measurements at lower and higher redshifts, and provides the most precise $z = 0.62$ SFRD measurement yet.

We have also presented a distribution of Hα emitters' sizes and show how the objects' half-light radii correlate with their Hα luminosities.

REFERENCES

Bertin, E., & Arnouts, S. 1996, A&AS, 117, 393

Calzetti, D., Bohlin, R. C., Kinney, A. L., Storchi-Bergmann, T., & Heckman, T. M. 1995, ApJ, 443, 136

Capak, P., Aussel, H., Ajiki, M., et al. 2007, ApJS, 172, 99

Cappelluti, N., Brusa, M., Hasinger, G., et al. 2009, A&A, 497, 635

Civano, F., Marchesi, S., Comastri, A., et al. 2016, ApJ, 819, 62

Coil, A. L., Blanton, M. R., Burles, S. M., et al. 2011, ApJ, 741, 8

Cool, R. J., Moustakas, J., Blanton, M. R., et al. 2013, ApJ, 767, 118

Dale, D. A., Barlow, R. J., Cohen, S. A., et al. 2010, ApJ, 712, L189

Gómez-Guijarro, C., Gallego, J., Villar, V., et al. 2016, A&A, 591, A151

Hayes, M., Schaerer, D., & Östlin, G. 2010, A&A, 509, L5

Hopkins, A. M., Connolly, A. J., Haarsma, D. B., & Cram, L. E. 2001, AJ, 122, 288

Ilbert, O., Capak, P., Salvato, M., et al. 2009, ApJ, 690, 1236

Kennicutt, Jr., R. C. 1998, ARA&A, 36, 189

Laigle, C., McCracken, H. J., Ilbert, O., et al. 2016, ApJS, 224, 24

Laureijs, R., Amiaux, J., Arduini, S., et al. 2011, ArXiv e-prints, arXiv:1110.3193

Leauthaud, A., Massey, R., Kneib, J.-P., et al. 2007, ApJS, 172, 219

Lilly, S. J., Le Fèvre, O., Renzini, A., et al. 2007, ApJS, 172, 70

Lilly, S. J., Le Brun, V., Maier, C., et al. 2009, ApJS, 184, 218

Ly, C., Lee, J. C., Dale, D. A., et al. 2011, ApJ, 726, 109

Madau, P., & Dickinson, M. 2014, ARA&A, 52, 415

McCracken, H. J., Milvang-Jensen, B., Dunlop, J., et al. 2012, A&A, 544, A156

Probst, R. G., George, J. R., Daly, P. N., Don, K., & Ellis, M. 2008, 7014, 2

Probst, R. G., Gaughan, N., Abraham, M., et al. 2004, 5492, 1716

Schechter, P. 1976, ApJ, 203, 297

Sobral, D., Smail, I., Best, P. N., et al. 2013, MNRAS, 428, 1128

Spergel, D., Gehrels, N., Baltay, C., et al. 2015, ArXiv e-prints, arXiv:1503.03757

Swaters, R. A., Valdes, F., & Dickinson, M. E. 2009, in Astronomical Society of the Pacific Conference Series, Vol. 411, Astronomical Data Analysis Software and Systems XVIII, ed. D. A. Bohlender, D. Durand, & P. Dowler, 506

Trenti, M., & Stiavelli, M. 2008, ApJ, 676, 767

Villar, V., Gallego, J., Pérez-González, P. G., et al. 2008, ApJ, 677, 169

Wang, B., & Heckman, T. M. 1996, ApJ, 457, 645

Wright, E. L. 2006, PASP, 118, 1711